Quantifying permafrost deformation with ICESat-2

R. J. Michaelides[*,1], **M. Bryant**[*,2], **M. R. Siegfried**[1], **A. A. Borsa**[2]

[1]Department of Geophysics, Colorado School of Mines, Golden, CO USA

[2]Institute of Geophysics and Planetary Physics, Scripps Institution of Oceanography, University of California, San Diego, La Jolla, CA USA

*Contributed equally to the manuscript

Key Points:

- We demonstrate that ICESat-2 altimetry can successfully resolve surface subsidence due to seasonally thawing permafrost
- ICESat-2 measurements of surface deformation are broadly consistent with independently-derived deformation estimates from Sentinel-1 InSAR
- The complementarity of ICESat-2 laser altimetry and InSAR methods shows promise for novel investigations of permafrost surface dynamics

Corresponding author: Roger J. Michaelides, `michaelides@mines.edu`

Abstract

We use ICESat-2 laser altimetry crossovers and repeat tracks collected over the North Slope of Alaska to estimate height change due to the deformation of seasonally freezing and thawing permafrost. We compare these measurements with a time series of surface deformation from Sentinel-1 interferometric synthetic aperture radar (InSAR) and demonstrate agreement between these independent observations of surface deformation. Both methods resolve pronounced surface subsidence during the 2019 thaw season within the 2007 Anaktuvuk River fire scar. A temporal relationship between measured surface subsidence/uplift and changes in normalized annual degree days is observed, consistent with the thermodynamically driven seasonal freezing and thawing of the active layer. We discuss optimal strategies of post-processing ICESat-2 data for permafrost applications, as well as the future potential of joint ICESat-2 and InSAR investigations of permafrost surface dynamics.

Plain Language Summary

NASA's Ice, Cloud, and Land Elevation Satellite (ICESat-2) was designed to accurately measure surface heights so that changes on ice sheets, sea ice, and biomass might be studied. In this paper, we demonstrate the ICESat-2 can be successfully employed in permafrost regions, where seasonal freezing and thawing of frozen ground causes the Earth's surface to deform with time. By comparing changes in estimated height from the ICESat-2 satellite, we can quantify the amount of surface deformation that occurs over a study site on the Alaskan North Slope. We compare these estimates of surface deformation with independent estimates of surface deformation acquired by the European Space Agency's Sentinel-1 spacecraft, which was specifically designed to precisely measure surface deformation. By comparing these independent measurements from two satellites, we demonstrate that agreement of the estimated spatial patterns of surface deformation, suggesting that ICESat-2 can be used to quantify surface dynamics in permafrost regions.

1 Introduction

Permafrost, defined as ground that remains frozen for two or more consecutive years, underlies 24% of the Northern Hemisphere, and contains stores of bound carbon in the subsurface (primarily carbon dioxide and methane) amounting to 60% of the world's soil

carbon (Turetsky et al., 2020). The Arctic, where the majority of permafrost is located, is the fastest changing component of the global climate system, with air temperatures across the Arctic currently increasing at roughly twice the average global rate (Jorgenson et al., 2001). Rising air temperatures can increase the magnitude of seasonal thawing and freezing of the uppermost portion of the permafrost column (the "active layer") and can induce permanent melting and unrecoverable loss of permafrost. Both of these processes can result in decomposition of bound soil carbon and its release into the atmosphere (Natali et al., 2019). Results from the Coupled Model Intercomparison Project Phase 5 (CMIP5) suggest that global permafrost extent may decrease anywhere from 20–37% by the end of the 21st century (Wang et al., 2019). As simultaneously one of the largest carbon reservoirs in the global carbon cycle and one of the fastest-warming regions on Earth, permafrost plays a disproportionately large role in the global climate system. Consequently, robust and expansive monitoring of regions with changing permafrost will be essential through the 21st century.

The Circumpolar Active Layer Monitoring Network (CALM) was established in 1991 to observe long-term, interannual impacts of variable climate on the active layer and near-surface permafrost (Brown et al., 2000). More recently, Global Navigation Satellite System (GNSS) reflectometry has been used to resolve both annual and inter-annual surface deformation associated with thawing of the active layer (Liu & Larson, 2018; Hu et al., 2018). Although GNSS and dedicated in-situ monitoring efforts like CALM can provide precise estimates of permafrost subsidence, these are point measurements that may not adequately represent permafrost changes away from the point of observation. The vastness of permafrost regions and the general inaccessibility of much of the northern high latitudes hamper many conventional methods of in situ monitoring. As a result, remote sensing techniques such as visual (e.g., Quinton et al., 2010) or multispectral (e.g., Nitze & Grosse, 2016) imagery mapping, lidar surveying (e.g., Jones et al., 2013), and synthetic aperture radar (SAR) analysis (e.g., Liu et al., 2010), have been employed to monitor permafrost, with varying degrees of success.

Interferometric synthetic aperture radar (InSAR) is a geodetic technique that can resolve centimetric deformation of the Earth's surface (e.g., Goldstein & Zebker, 1987; Rosen et al., 2000). InSAR has been successfully applied to study a range of phenomena in permafrost regions that give rise to surface deformation, including seasonal thawing of the active layer (Liu et al., 2012), wildfire-induced thermokarst (Liu et al., 2014),

initiation of retrogressive thaw slumps (Zwieback et al., 2018), and post-wildfire active layer thaw and recovery (Michaelides et al., 2019). Although InSAR processing is capable of resolving deformation over vast spatial extents, precise estimates of deformation require several repeat observations and interferometric coherence from image to image. Extensive vegetation cover, changes in surface water cover, extent, and saturation, and variable snow cover, all of which are ubiquitous phenomena in permafrost regions, can induce signal decorrelation over temporal baselines as short as several weeks and limit the precision with which InSAR analysis can determine deformation in permafrost regions.

The launch of the Ice, Cloud, and land Elevation Satellite 2 (ICESat-2) mission (Markus et al., 2017) in September 2018 provides an opportunity to complement InSAR techniques with spaceborne laser altimetry that extends to ±88° latitude. The small footprint, fine-scale along-track spacing, and high precision of elevation retrievals (e.g., B. Smith et al., 2020) suggests that ICESat-2 data products should be of sufficient quality to estimate surface deformation in complex permafrost terrain. Whereas C-band InSAR decorrelates across temporal baselines longer than a few weeks, ICESat-2 can yield long-period temporal information without signal degradation. Similarly, InSAR and laser altimetry are sensitive to different atmospheric characteristics, providing complementary observations of permafrost evolution and hazards in a challenging atmospheric environment. In this work, we demonstrate the capability of the ICESat-2 mission to quantify spatial patterns of active-layer deformation of permafrost in Arctic Alaska on the order of centimeters to decimeters. We compare our ICESat-2 results to InSAR-derived models of active-layer subsidence to validate our ICESat-2 retrievals and finally suggest future steps for expanding ICESat-2 data analysis to pan-Arctic estimates of Arctic permafrost change.

2 Methods

2.1 Field Site

We compare Sentinel-1 InSAR deformation and ICESat-2 height change in a 3220 km^3 region of the North Slope of Alaska that encompasses the foothills of the Brooks Range to the south and the Arctic coastal plain to the north (Figure 1). Although the southern reaches of the study region exhibit considerable topographic relief, the tundra to the North of the foothills is flat and characterized by heath vegetation, tussock tun-

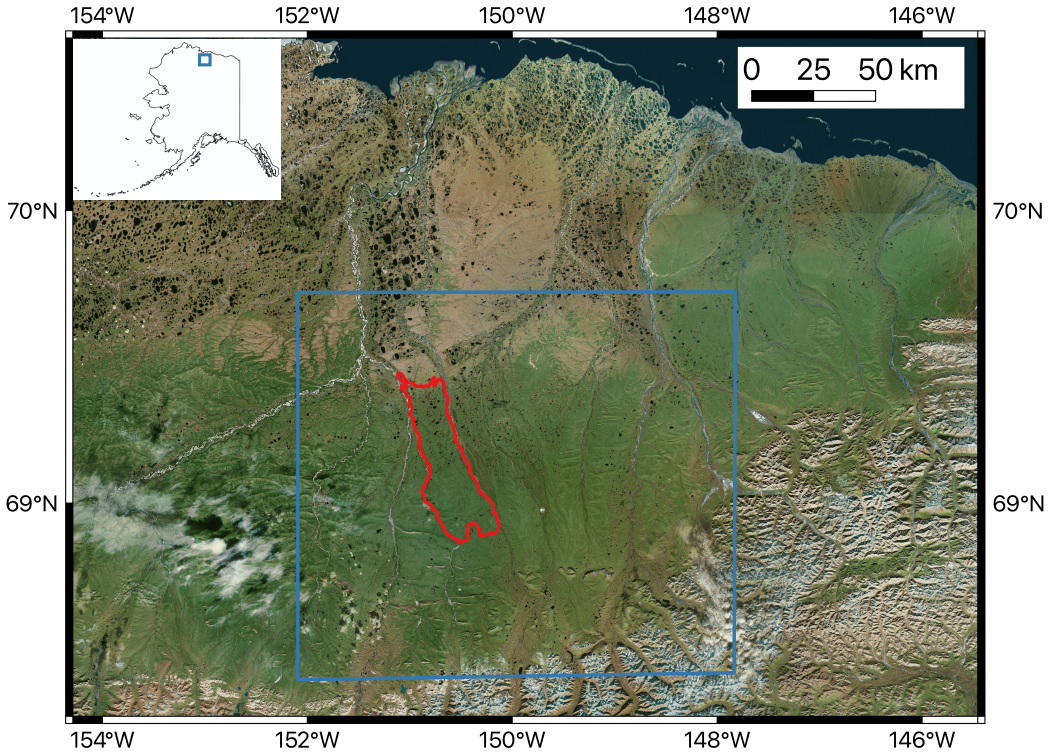

Figure 1. Study site within the Alaskan North Slope, with relative position within Alaska (inset). The bounding box of the comparison between Sentinel InSAR and ICESat-2 data is shown in blue and the 2007 Anaktuvuk River fire scar is highlighted in red.

dra, and wet sedge tundra along well-drained hilltops, hillslopes, and saturated lowland valleys, respectively (J. Chen et al., 2020). The entirety of the Alaskan North Slope is underlain by continuous permafrost, with reported active layers ranging from 40 cm to 100 cm in depth (Brown et al., 2000).

Ignited by a lightning strike on 16 July 2007, the Anaktuvuk River fire burned ~1039 km^2 of tundra in our study region, resulting in a doubling of the cumulative burned area of the Alaskan North Slope over the last 50 years (Jones et al., 2009) and a release of ~2.1 Tg of carbon into the atmosphere—equivalent to the net annual carbon sink of the circumpolar Arctic tundra (Mack et al., 2011). Both field measurements and InSAR measurements have indicated post-fire increases in active layer thickness and seasonal subsidence of the tundra burned by the Anaktuvuk River fire (Rocha & Shaver, 2011; Liu et al., 2014).

2.2 InSAR

We use SAR data acquired between 7 Jan. 2019 and 21 Dec. 2019 by the Sentinel-1A satellite, which operates at C-band (∼5.65 cm wavelength) and with a 12-day temporal repeat in the high Arctic. We processed raw data (L1.0) collected in the interferometric wide swath (IWS) mode using the 'geocoded single-look complex' (SLC) back-projection method (H. A. Zebker & Zheng, 2016; Zheng & Zebker, 2017). All SLC radar images were coregistered to a digital elevation model (DEM) spanning the region of interest and produced from the photogrammetric ArcticDEM dataset (Porter et al., 2018). The DEM was downsampled to a resolution of ∼5 m by ∼15 m, to match the native 5 m by 15 m spatial resolution of the Sentinel-1A satellite in range and azimuth, respectively.

We generated a network of interferograms from all coregistered SLCs using a temporal baseline of 48 days and a perpendicular baseline of 150 m. We took 18 looks in range and 6 looks in azimuth during interferogram formation to increase the signal-to-noise ratio (SNR) of the phase estimation, resulting in interferograms with a spatial resolution of ∼100 m in both range and azimuth. We then unwrapped all interferograms using the SNAPHU algorithm (C. W. Chen & Zebker, 2001). We used the correlation files of each interferogram to aid in the unwrapping scheme and tiled each interferogram to speed up computational time. We then applied a unimodal correction to all unwrapped interferograms to correct for any phase unwrapping errors in the unwrapped interferograms. All interferograms exhibiting severe decorrelation or turbulent atmospheric noise were removed from the set of interferograms used for analysis. The topography-correlated component of atmospheric noise was empirically removed from all interferograms using the DEM following Doin et al. (2009). Due to the paucity of reliable GNSS stations in the study region, all interferograms were phase-referenced using a selection of several pixels exhibiting high coherence in regions of no assumed deformation (i.e., mountain ridges) following Liu et al. (2012).

After applying the above calibrations to the InSAR data, we generated a pixel-wise time-series across the comparison region using the small baseline subset (SBAS) method (Berardino et al., 2002). The SBAS method is an inversion that solves for the pixel-by-pixel instantaneous velocity at the time of each SAR image acquisition. The estimated velocities were then integrated through time to form a time-series of surface displacements for each pixel over the temporal range of the network of input interferograms.

2.3 ICESat-2

ICESat-2 is in a polar orbit with a 92° inclination, collecting observations from 88°N to 88°S with a 91-day exact repeat (Markus et al., 2017). ICESat-2's laser instrument emits a single pulse, which is split into 3 pairs of beams, where each pair has one strong beam that is four times stronger than the corresponding weak beam. The three pairs are spaced at ∼3.3 km across-track and beams within a pair are spaced at ∼90 m, with the exact geometry controlled by spacecraft attitude (Neumann et al., 2019).

Each beam illuminates a surface spot of 12–15 m diameter (Klotz et al., 2020) every 0.7 m along track. During the period covered by this study, ICESat-2 operated in "mapping mode" away from polar regions, , resulting in a higher density of tracks but no repeat measurements (Neumann et al., 2019). However, since the North Slope of Alaska is "target of opportunity" for the ICESat-2 mission, every fifth descending track was repeated. This resulted in a small number of repeated tracks during the 2019 thaw season that is the focus of our study. We note that on 9 Sep. 2019, the satellite performed a yaw flip in which the orientation of the altimeter instrument, and thus the relative ordering of weak and strong beams, was reversed.

We used surface height estimates from the Land Ice Height Product, ATL06 (B. E. Smith et al., 2019). ATL06 processing filters and provides a linear fit to the geolocated surface photons along 50%-overlapping 40 m segments to estimate the centroid height and surface slope in the along-track and across-track directions (B. Smith et al., 2019). We only used ATL06 data points flagged as high quality and that had a height within 2 m of adjacent segments. In addition, we removed segments with surface height uncertainty >1 m, along-track slope >5 degrees, and a signal-to-noise ratio significance level <0.02.

We estimated surface height changes from both repeated tracks and profile crossover points. To identify crossing locations, we divided the study area into 10 km latitudinal bands. Within each band, we fit lines to the longitude and latitude coordinates of ATL06 segments on individual tracks and calculated all intersections. Using this method, we compared 291 profiles and identified 9839 potential crossovers. For each crossover, we then constrained the data from the crossing tracks to segments lying within a specified radius of the crossing location. We considered the crossover valid if the track had a density of at least 1 point every 40 m, then recalculated the precise crossover location using these local segments .We estimated the profile heights at the crossover location using a line

fit to ATL06 segment heights as a function of along-track distance. Finally, we estimated the crossover height difference (dH) as the difference of the profile elevations at the crossover location, subtracting the later observation in time from the earlier observation. We propagated uncertainties on individual ATL06 elevations through to the final dH estimates.

To examine the sensitivity of our crossover estimation to our choice of input data, we tested interpolation distances ranging from 20 m to 100 m for fitting lines to ATL06 segments on either side of the crossover location. For this analysis, we used crossovers with a time interval of 14 days or less, a period over which we assume surface height change is negligible.

We identified potential repeat tracks by flagging tracks from the same RGT with different collection dates and corresponding beams had an across-track distance difference of <45 m. For each point from the earlier profile, we identified the closest point on the later profile and calculated the distance between observations. In order to ensure sufficiently overlapping segments, we only kept pairs that were within 5 m of each other across-track. We then calculated the height difference between each pair. In order to reduce the noise in our final results, we applied a boxcar filter over 2 km. Through this process we identified four RGTs with repeat profiles and consistent collection across the region of interest, including three 182-repeats and one 91-day repeat. Seven additional tracks had sparse coverage, likely due to cloud cover. We selected the 91-day repeat track (RGT 1280) and one of the 182-day repeats tracks (RGT 335) for direct comparison with the InSAR results.

3 Results and Discussion

3.1 InSAR Deformation

We applied the SBAS algorithm to 14 interferograms spanning the 2019 thaw season. The SBAS algorithm solves for a time series of instantaneous velocity estimates for each epoch at which a SAR image was acquired. Integrating this velocity time series yields a time series of surface deformation, which can be directly compared to all deformation estimates derived from ICESat-2. The SBAS method resolves increased subsidence over the 2007 Anaktuvuk River fire scar (red outline, Figure 1). We observe a ∼1.5 cm difference in subsidence between the burned tundra and unburned tundra, which is con-

sistent with estimates of 12 year post-fire active layer recovery from the Yukon-Kuskokwim delta (Michaelides et al., 2019).

3.2 ICESat-2 Height Change

We compared 291 individual ICESat-2 beams on ascending and descending tracks spanning the 2019 thaw season, yielding between 785 and 975 crossovers with the required point density, depending on the interpolation radius. The crossovers spanned time periods ranging from 3 to 218 days, with 120 129 "short-period" crossovers spanning 14 days or less. Figure 2 shows the standard deviation of short-period crossovers and median propagated uncertainty (1σ) as a function of radius. The median standard deviation increases sharply with interpolation distance. Although we would expect interpolations over longer length scales to reduce the uncertainty for flat areas, the topography in this region is complex, leading to high residuals when interpolating over several ATL06 segments. Both the uncertainty and short-period standard deviation are minimized for the 20 m interpolation, with a median uncertainty of 1.9 cm across all estimates and a standard deviation of 14 cm for the 120 short-period crossovers. Therefore, we conclude that interpolation using only the nearest two points is the optimal solution given the terrain.

Crossovers height changes (dH) from the entire thaw season indicate net subsidence across the region, with elevation changes ranging from -156 to 83 cm, a median of -19 cm, and uncertainties ranging up to 94 cm. The subset of short-period crossovers indicate large crossover variability. While the median bias of short-period crossovers is a small -0.15 cm , individual estimates vary from -47 cm to 36 cm.

The 11 total repeat tracks in this study yielded height changes ranging from -550 to 350 cm, with uncertainties between 0.8 and 97 cm. Overall, repeat-track comparisons show net subsidence over the study region, with a mean of -29 cm. As expected, the magnitude of height change from 181-day repeat tracks are higher (-550 cm $< dH <$ 350 cm; 1.5 cm $< \sigma <$ 97 cm) than that for the 91-day repeats (-270 cm $< dH <$ 230 cm; 0.81 cm $< \sigma_i <$ 95 cm). We selected one 91-day repeat (RGT 1280) and one 182-day repeat (RGT 0335) for comparison to the InSAR results. Applying the 2 km boxcar filter reduces both the spread and the uncertainty in the data. For RGT 0335 spot 2l, this reduces the standard deviation and median uncertainty from 43 cm and 6.4 cm to 30 cm

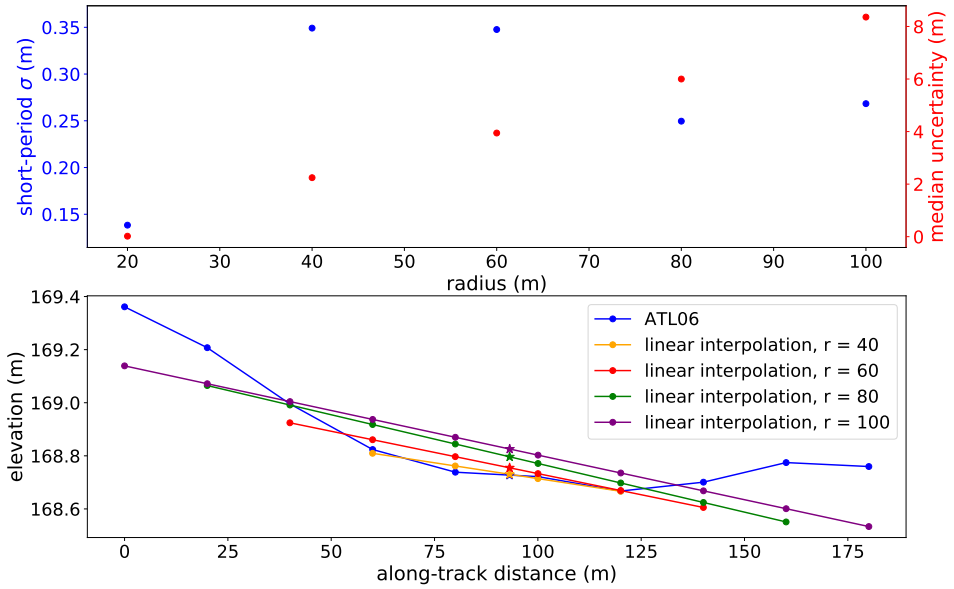

Figure 2. Top: standard deviation of short-period (<14 days) crossovers (left axis) and median propagated uncertainty (right) as a function of interpolation radius. Bottom: an example of linear fitting of an ATL06 profile in this region. As the interpolation radius increases, the interpolation does a poorer job of fitting the surface, and the crossover height estimate deviates further from the true surface.

and 0.8 cm respectively. For track 1280 spot 2l, this reduces the standard deviation and median uncertainty from 21 cm and 6.4 cm to 12 cm and 1.3 cm. The spatial distribution of the averaged dH values for each of the two RGTs is shown in figure 3.

3.3 Comparison Between Techniques

Due to the large amount of noise in the crossover estimates (as indicated by the short-period crossovers), a direct comparison between crossovers and InSAR estimates is challenging. However, by comparing crossover-derived height changes to their associated changes in normalized accumulated degree days (NADD)–which were calculated from NASA's Daily Surface Weather and Climatological Summaries (DAYMET) reanalysis temperature dataset–a clear temporal correlation emerges. The magnitude (sign) of ICESat-2-derived vertical surface deformation is positively (negatively) correlated with

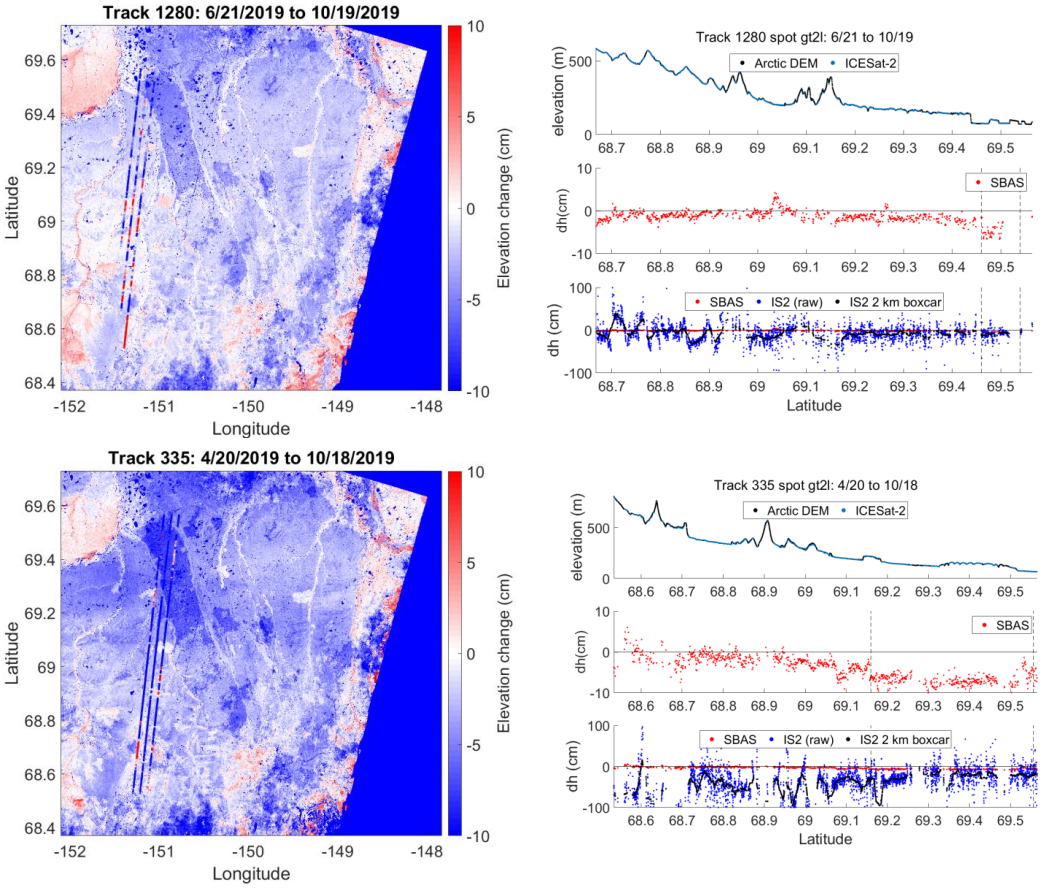

Figure 3. Left: comparison of the elevation changes from 91-day (RGT 1280) and 182-day (RGT 0335) repeat tracks, as well as the SBAS deformation estimate over a similar time period. Right: along-track profiles of the ICESat-2 raw (yellow) and boxcar-filtered (purple) elevation changes for spot 2l of each track, and the SBAS-derived estimates (red) of the deformation over that time interval. The vertical dashed line indicates the latitudinal bounds of the burn area.

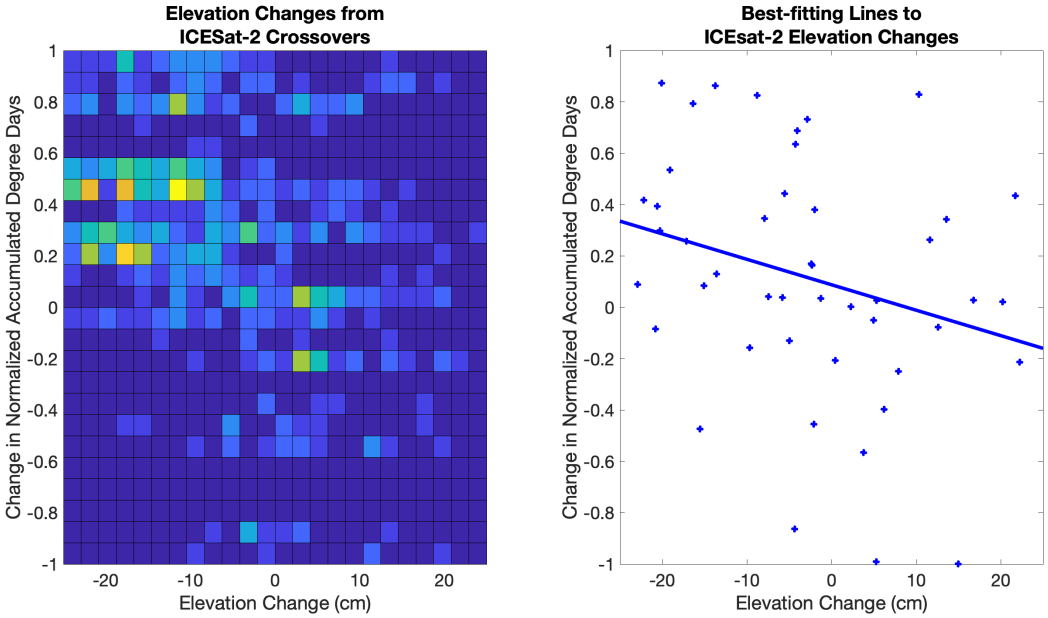

Figure 4. Left: Two-dimensional histogram of ICESat-2 crossover height-change estimates and the associated change in normalized accumulated degree days (NADD). Right: The linear best fit to the histogram to the data in the left panel.

the magnitude (sign) of NADD change (Figure 4). This relationship is physically consistent with active layer thawing (subsidence) during time spans where degree days accumulate– warming summer months– and freeze-up (uplift) during active layer freezing, when changes in degree days are negative.

To validate ICESat-2 permafrost deformation estimates from repeat tracks, we compare our ICESat-2 height-change estimates to SBAS-derived deformation over approximately the same temporal baseline. Figure 3) displays the SBAS-derived deformation observed between dates 23 Jun. 2019 and 16 Sep. 2019, with ICESat-2-derived 91-day height change from RGT 1280, which spanned 06 Jun 2019 and 19 Oct 2019 overlain. We also show the comparison between SBAS deformation between 20 Apr 2019 and 23 Oct 2019 and 182-day height change on RGT 0335, which spanned 04 Apr 2019 and 18 Oct 2019. The difference in acquisition date between the first ICESat-2 and Sentinel images and second ICESat-2 and Sentinel images is 3 days for RGT 1280 and 5-6 days for RGT 0335, such that the expected deformation of the surface between the inter-instrument image acquisition can be assumed small. As such, the surface deformation observed by InSAR and ICESat-2 are expected to be roughly equivalent.

Whereas ICESat-2 observes systematically larger elevation changes than InSAR, both the spatial pattern and sign of observed elevation change (i.e., uplift or subsidence) is consistent with InSAR observations. Notably, both Sentinel-1 and ICESat-2 observed increased subsidence over the 2007 Anaktuvuk River fire scar compared to nearby unburned tundra. Additionally, both methods observe an inverse correlation between topography and subsidence, with well-saturated lowlands exhibiting larger subsidence than well-drained hill slopes and ridge crests, consistent with past studies (J. Chen et al., 2020). Anomalously large uplift values are inferred from ICESat-2 crossovers over topographically rough surfaces (such as exposed rock ridge tops) and several rivers and river floodplains. These large-magnitude values are likely related to errors in our interpolation over rough terrain or failure of the ATL06 assumption that over 40 m length scales, the surface topography can be estimated as a plane, suggesting a higher level surface-height data product that considers the unique topographic and roughness characteristics of permafrost regions would improve ICESat-2's utility for long-term thaw monitoring. Deformation estimates from the 182-day repeat are systematically higher than those from the 91-day repeat. This discrepancy is likely predominantly due to the fact that the 182-day repeat spans the entire thaw season, while the 91-day repeat does not. However, height changes due to late spring snow melt may also be contained within the 182-day deformation measurement. If ICESat-2 is indeed sensitive to changes in snow height, it may prove complementary to InSAR-based studies of late spring thaw, which can be severely impacted by signal decorrelation.

Sentinel-1 InSAR, ICESat-2 crossovers, and ICESat-2 repeat-track methods capture spatially consistent patterns of surface deformation associated with subsidence of the thawing active layer. However, ICESat-2 measurements are systematically larger and noisier than InSAR measurements, and require along-track filtering with a boxcar impulse response on the order of 100 segments (2 km) to derive comparable deformation estimates to the InSAR results. This discrepancy may be partially due to both the operational nature of the two imaging techniques, as well as their respective post-processing methods. Although synthetic aperture radar interferometry and laser altimetry are both coherent source imaging techniques, the physical nature of each instrument's backscattered signal is different. SAR backscatter represents a convolution of the output radar signal with the distribution of scattering elements contained within each ground resolution element (resel). The distribution of scattering elements within any one individ-

ual resel may result in a noisy phase estimate, but considerable spatial averaging ("multilooking") in both the along-track and across-track of the radar image results in a larger signal-to-noise ratio (SNR) and more precise phase estimate (Goldstein et al., 1988; Li & Goldstein, 1990; H. Zebker & Villasenor, 1992). Starting from SAR images with a native resolution of ∼5 m by ∼15 m across-track and along-track, respectively, a total of 18 looks across-track and 6 looks along-track were taken during interferogram image formation to generate images with a 100 m spatial resolution in both along-track and cross-track. As such, each individual phase estimate represents a statistical average of 108 independent measurements. In contrast, the ICESat-2 ATL06 dataset has a native along-track resolution of 40 m. The altimetric return from the ICESat-2 laser is dictated by the count density of backscattered photons, which is typically <10 signal photons out of 200 trillion transmitted photons (Neumann et al., 2019). Although the deformation uncertainty of a native resolution InSAR pixel is on the order of 1 cm, ATL06 height estimates have a precision of 9 cm for best-case targets (high reflectivity; low roughness) (Brunt et al., 2019), and any inferred deformation (i.e., change in height) will be even larger. Therefore, an even greater number of statistical averages is likely necessary to achieve height-change estimates from ICESat-2 with the precision of InSAR methods.

Moreover, because ICESat-2 provides a one-dimensional, along-track measurement rather than a two-dimensional image like SAR, achieving a comparable number of statistical samples as a 100 m InSAR pixel necessitates boxcar-filtering ICESat-2 data in the along-track direction with a spatial resolution of ∼2 km. As such, InSAR and ICESat-2 estimates of deformation will agree better in flatter regions such as the northern Arctic coastal plain, where topographically rough areas like the Brooks Range foothills exhibit larger differences in inferred deformation. Therefore, a large amount of along-track filtering over complicated topography will break assumptions of signal ergodicity, and may result in biased estimates of deformation with large uncertainties. The ATL06 data product was designed primarily for surface slopes of 1° or less (B. Smith et al., 2019), whereas slopes in this region are often a few degrees or more. We only included height changes for areas with surface slopes less than 5°,however stricter surface slope restrictions may be needed. Alternatively, uncertainties in ICESat-2 derived deformations might be lowered by adaptively varying the crossover interpolation and along-track smoothing based upon local topography.

ICESat-2 can retrieve estimates of surface deformation that are qualitatively in agreement–particularly in terms of spatial structure–with independent InSAR estimates, but achieving this result requires appropriate statistical averaging and is expected to work better in regions exhibiting more uniform surface topography and permafrost distribution at the km spatial scale. In regions that exhibit a large degree of spatial heterogeneity, the assumptions of signal ergodicity inherent to any statistical averaging techniques break down, and biases in estimated deformation can manifest. Additionally, the complex roughness characteristics of tundra terrains–particularly tussock tundra–can introduce uncertainties in the ICESat-2 height retrieval itself, as photons may backscatter from vegetation scattering elements distributed over several decimeters. The smaller native precision of interferometric measurements, as well as the two-dimensional nature of InSAR images, makes InSAR measurements more robust to spatial variability than ICESat-2. Nonetheless, we have demonstrated a noticeable sensitivity of ICESat-2 to local-scale deformation associated with seasonal permafrost thawing, which necessitates future investigation into the full potential of ICESat-2 observations for characterization of permafrost surface dynamics. Coherent ICESat-2 repeat and crossover estimates at 91 and 182 day intervals complement the ubiquitous problem of interferometric temporal decorrelation that plagues InSAR-based studies in permafrost regions. Furthermore, these two methods can also look at complementary targets: whereas the sidelooking viewing geometry of conventional SAR imaging systems makes them insensitive to surface water bodies, the nadir geometry of ICESat-2 might allow for precise estimates of surface water height levels and changes. Such measurements, combined with InSAR-based measurements of surface subsidence and active layer thickness, could allow for novel investigations of the spatiotemporal relationships between permafrost thaw, water table and lake/river level heights, as well as potentially the horizontal flow of groundwater through the permeable active layer.

4 Summary

This study provides a preliminary investigation into the effectiveness of using ICESat-2 height changes to study permafrost thaw subsidence. We compared ICESat-2-derived surface deformation over a 91-day and a 182-day interval across a region of the North Slope, Alaska, to InSAR-derived subsidence. We found that, although the magnitudes of deformation differ between ICESat-2 and InSAR retrievals, the longer-wavelength spa-

tial structures of deformation are similar, indicating that the two instruments are sensitive to large-scale subsidence patterns. Furthermore, both crossovers and repeat tracks are capable of detecting large-scale subsidence patterns over the thaw season, although additional repeat-track data collection is necessary to better assess the short-scale noise characteristics of ICESat-2 altimetry over permafrost. The uncertainty in ICESat-2-based deformation estimates seems to be primarily due to the complicated topography and scattering physics of vegetated tundra. Thus, it may be possible to refine ICESat-2 estimates of surface deformation by limiting analysis to topographically smooth areas, or by developing adaptive algorithms that account for more local topography variations during statistical averaging. Further investigation into the fundamental nature of the scattering physics which gives rise to radar backscatter and photon backscatter over tundra terrain is also warranted. Given the importance of permafrost dynamics to the global carbon cycle, we advocate for investigation into the full potential of using ICESat-2 data products to quantify surface dynamics in permafrost and periglacial environments.

Acknowledgments

This work was partially funded by NASA Grant 80NSSC19K1640. Copernicus Sentinel data collected in 2019 was retrieved from ASF DAAC on 6 July 2020, processed by ESA. ICESat-2 data are available via NSIDC (https://nsidc.org/data/atl06). DEMs provided by the Polar Geospatial Center under NSF OPP awards 1043681, 1559691 and 1542736.

References

Berardino, P., Fornaro, G., Lanari, R., & Sansosti, E. (2002, nov). A new algorithm for surface deformation monitoring based on small baseline differential SAR interferograms. *IEEE Transactions on Geoscience and Remote Sensing*, *40*(11), 2375–2383. Retrieved from `https://doi.org/10.1109/tgrs.2002.803792` doi: 10.1109/tgrs.2002.803792

Brown, J., Hinkel, K. M., & Nelson, F. E. (2000, jul). The circumpolar active layer monitoring (calm) program: Research designs and initial results1. *Polar Geography*, *24*(3), 166–258. Retrieved from `https://doi.org/10.1080/10889370009377698` doi: 10.1080/10889370009377698

Brunt, K. M., Neumann, T. A., & Smith, B. E. (2019, nov). Assessment of ICESat-2 Ice Sheet Surface Heights, Based on Comparisons Over the Inte-

rior of the Antarctic Ice Sheet. *Geophysical Research Letters*, *46*(22), 13072–13078. Retrieved from https://doi.org/10.1029\%2F2019gl084886 doi: 10.1029/2019gl084886

Chen, C. W., & Zebker, H. A. (2001, feb). Two-dimensional phase unwrapping with use of statistical models for cost functions in nonlinear optimization. *Journal of the Optical Society of America A*, *18*(2), 338. Retrieved from https://doi.org/10.1364/josaa.18.000338 doi: 10.1364/josaa.18.000338

Chen, J., Wu, Y., O'Connor, M., Cardenas, M. B., Schaefer, K., Michaelides, R., & Kling, G. (2020). Active layer freeze-thaw and water storage dynamics in permafrost environments inferred from InSAR. *Remote Sensing of Environment*, *248*, 112007. Retrieved from https://doi.org/10.1016/j.rse.2020.112007 doi: 10.1016/j.rse.2020.112007

Doin, M.-P., Lasserre, C., Peltzer, G., Cavalié, O., & Doubre, C. (2009, sep). Corrections of stratified tropospheric delays in SAR interferometry: Validation with global atmospheric models. *Journal of Applied Geophysics*, *69*(1), 35–50. Retrieved from https://doi.org/10.1016/j.jappgeo.2009.03.010 doi: 10.1016/j.jappgeo.2009.03.010

Goldstein, R. M., & Zebker, H. A. (1987, aug). Interferometric radar measurement of ocean surface currents. *Nature*, *328*(6132), 707–709. Retrieved from https://doi.org/10.1038/328707a0 doi: 10.1038/328707a0

Goldstein, R. M., Zebker, H. A., & Werner, C. L. (1988, jul). Satellite radar interferometry: Two-dimensional phase unwrapping. *Radio Science*, *23*(4), 713–720. Retrieved from https://doi.org/10.1029/rs023i004p00713 doi: 10.1029/rs023i004p00713

Hu, Y., Liu, L., Larson, K. M., Schaefer, K. M., Zhang, J., & Yao, Y. (2018, jun). GPS Interferometric Reflectometry Reveals Cyclic Elevation Changes in Thaw and Freezing Seasons in a Permafrost Area (Barrow, Alaska). *Geophysical Research Letters*, *45*(11), 5581–5589. Retrieved from https://doi.org/10.1029/2018gl077960 doi: 10.1029/2018gl077960

Jones, B. M., Kolden, C. A., Jandt, R., Abatzoglou, J. T., Urban, F., & Arp, C. D. (2009, aug). Fire Behavior, Weather, and Burn Severity of the 2007 Anaktuvuk River Tundra Fire, North Slope, Alaska. *Arctic, Antarctic, and Alpine Research*, *41*(3), 309–316. Retrieved from https://doi.org/10.1657/

1938-4246-41.3.309 doi: 10.1657/1938-4246-41.3.309

Jones, B. M., Stoker, J. M., Gibbs, A. E., Grosse, G., Romanovsky, V. E., Douglas, T. A., ... Richmond, B. M. (2013, nov). Quantifying landscape change in an arctic coastal lowland using repeat airborne LiDAR. *Environmental Research Letters*, *8*(4), 045025. Retrieved from https://doi.org/10.1088/1748-9326/8/4/045025 doi: 10.1088/1748-9326/8/4/045025

Jorgenson, M. T., Racine, C. H., Walters, J. C., & Osterkamp, T. E. (2001). Permafrost degradation and ecological changes associated with a warming climate in central Alaska. *Climatic Change*, *48*(4), 551–579. doi: 10.1023/A:1005667424292

Klotz, B. W., Neuenschwander, A., & Magruder, L. A. (2020, jan). High-Resolution Ocean Wave and Wind Characteristics Determined by the ICESat-2 Land Surface Algorithm. *Geophysical Research Letters*, *47*(1). Retrieved from https://doi.org/10.1029/2019gl085907 doi: 10.1029/2019gl085907

Li, F., & Goldstein, R. (1990). Studies of multibaseline spaceborne interferometric synthetic aperture radars. *IEEE Transactions on Geoscience and Remote Sensing*, *28*(1), 88–97. Retrieved from https://doi.org/10.1109/36.45749 doi: 10.1109/36.45749

Liu, L., Jafarov, E. E., Schaefer, K. M., Jones, B. M., Zebker, H. A., Williams, C. A., ... Zhang, T. (2014, jun). InSAR detects increase in surface subsidence caused by an Arctic tundra fire. *Geophysical Research Letters*, *41*(11), 3906–3913. Retrieved from https://doi.org/10.1002/2014gl060533 doi: 10.1002/2014gl060533

Liu, L., & Larson, K. M. (2018, feb). Decadal changes of surface elevation over permafrost area estimated using reflected GPS signals. *The Cryosphere*, *12*(2), 477–489. Retrieved from https://doi.org/10.5194/tc-12-477-2018 doi: 10.5194/tc-12-477-2018

Liu, L., Schaefer, K., Zhang, T., & Wahr, J. (2012, jan). Estimating 1992-2000 average active layer thickness on the Alaskan North Slope from remotely sensed surface subsidence. *Journal of Geophysical Research: Earth Surface*, *117*(F1), n/a–n/a. Retrieved from https://doi.org/10.1029/2011jf002041 doi: 10.1029/2011jf002041

Liu, L., Zhang, T., & Wahr, J. (2010, aug). InSAR measurements of surface defor-

mation over permafrost on the North Slope of Alaska. *Journal of Geophysical Research*, *115*(F3). Retrieved from https://doi.org/10.1029/2009jf001547 doi: 10.1029/2009jf001547

Mack, M. C., Bret-Harte, M. S., Hollingsworth, T. N., Jandt, R. R., Schuur, E. A. G., Shaver, G. R., & Verbyla, D. L. (2011, jul). Carbon loss from an unprecedented Arctic tundra wildfire. *Nature*, *475*(7357), 489–492. Retrieved from https://doi.org/10.1038/nature10283 doi: 10.1038/nature10283

Markus, T., Neumann, T., Martino, A., Abdalati, W., Brunt, K., Csatho, B., ... Zwally, J. (2017, mar). The Ice, Cloud, and land Elevation Satellite-2 (ICESat-2): Science requirements, concept, and implementation. *Remote Sensing of Environment*, *190*, 260–273. Retrieved from https://doi.org/10.1016%2Fj.rse.2016.12.029 doi: 10.1016/j.rse.2016.12.029

Michaelides, R. J., Schaefer, K., Zebker, H. A., Parsekian, A., Liu, L., Chen, J., ... Schaefer, S. R. (2019, mar). Inference of the impact of wildfire on permafrost and active layer thickness in a discontinuous permafrost region using the remotely sensed active layer thickness (ReSALT) algorithm. *Environmental Research Letters*, *14*(3), 035007. Retrieved from https://doi.org/10.1088/1748-9326/aaf932 doi: 10.1088/1748-9326/aaf932

Natali, S. M., Watts, J. D., Rogers, B. M., Potter, S., Ludwig, S. M., Selbmann, A.-K., ... Zona, D. (2019, oct). Large loss of CO2 in winter observed across the northern permafrost region. *Nature Climate Change*, *9*(11), 852–857. Retrieved from https://doi.org/10.1038/s41558-019-0592-8 doi: 10.1038/s41558-019-0592-8

Neumann, T. A., Martino, A. J., Markus, T., Bae, S., Bock, M. R., Brenner, A. C., ... Thomas, T. C. (2019, nov). The Ice, Cloud, and Land Elevation Satellite – 2 mission: A global geolocated photon product derived from the Advanced Topographic Laser Altimeter System. *Remote Sensing of Environment*, *233*, 111325. Retrieved from https://doi.org/10.1016/j.rse.2019.111325 doi: 10.1016/j.rse.2019.111325

Nitze, I., & Grosse, G. (2016, aug). Detection of landscape dynamics in the Arctic Lena Delta with temporally dense Landsat time-series stacks. *Remote Sensing of Environment*, *181*, 27–41. Retrieved from https://doi.org/10.1016/j.rse.2016.03.038 doi: 10.1016/j.rse.2016.03.038

Porter, C., Morin, P., Howat, I., Noh, M.-J., Bates, B., Peterman, K., ... Bojesen, M. (2018). *ArcticDEM*. Harvard Dataverse. Retrieved from https://doi.org/10.7910/DVN/OHHUKH doi: 10.7910/DVN/OHHUKH

Quinton, W., Hayashi, M., & Chasmer, L. (2010, nov). Permafrost-thaw-induced land-cover change in the Canadian subarctic: implications for water resources. *Hydrological Processes*, *25*(1), 152–158. Retrieved from https://doi.org/10.1002/hyp.7894 doi: 10.1002/hyp.7894

Rocha, A. V., & Shaver, G. R. (2011, may). Postfire energy exchange in arctic tundra: the importance and climatic implications of burn severity. *Global Change Biology*, *17*(9), 2831–2841. Retrieved from https://doi.org/10.1111/j.1365-2486.2011.02441.x doi: 10.1111/j.1365-2486.2011.02441.x

Rosen, P., Hensley, S., Joughin, I., Li, F., Madsen, S., Rodriguez, E., & Goldstein, R. (2000, mar). Synthetic aperture radar interferometry. *Proceedings of the IEEE*, *88*(3), 333–382. Retrieved from https://doi.org/10.1109/5.838084 doi: 10.1109/5.838084

Smith, B., Fricker, H. A., Gardner, A. S., Medley, B., Nilsson, J., Paolo, F. S., ... Zwally, H. J. (2020, apr). Pervasive ice sheet mass loss reflects competing ocean and atmosphere processes. *Science*, *368*(6496), 1239–1242. Retrieved from https://doi.org/10.1126/science.aaz5845 doi: 10.1126/science.aaz5845

Smith, B., Fricker, H. A., Holschuh, N., Gardner, A. S., Adusumilli, S., Brunt, K. M., ... Siegfried, M. R. (2019, nov). Land ice height-retrieval algorithm for NASA's ICESat-2 photon-counting laser altimeter. *Remote Sensing of Environment*, *233*, 111352. Retrieved from https://doi.org/10.1016/j.rse.2019.111352 doi: 10.1016/j.rse.2019.111352

Smith, B. E., Fricker, H. A., Gardner, A., Siegfried, M. R., Adusumilli, S., Csathó, B. M., ... the ICESat-2 Science Team (2019). *ATLAS/ICESat-2 L3A Land Ice Height, Version 3*. Boulder, Colorado USA: NSDIC: National Snow and Ice Data Center. Retrieved from http://nsidc.org/data/atl06 doi: 10.5067/ATLAS/ATL06.003

Turetsky, M. R., Abbott, B. W., Jones, M. C., Anthony, K. W., Olefeldt, D., Schuur, E. A. G., ... McGuire, A. D. (2020, feb). Carbon release through abrupt permafrost thaw. *Nature Geoscience*, *13*(2), 138–143.

Retrieved from https://doi.org/10.1038/s41561-019-0526-0 doi: 10.1038/s41561-019-0526-0

Wang, C., Wang, Z., Kong, Y., Zhang, F., Yang, K., & Zhang, T. (2019, mar). Most of the Northern Hemisphere Permafrost Remains under Climate Change. *Scientific Reports*, *9*(1). Retrieved from https://doi.org/10.1038/s41598-019-39942-4 doi: 10.1038/s41598-019-39942-4

Zebker, H., & Villasenor, J. (1992). Decorrelation in interferometric radar echoes. *IEEE Transactions on Geoscience and Remote Sensing*, *30*(5), 950–959. Retrieved from https://doi.org/10.1109/36.175330 doi: 10.1109/36.175330

Zebker, H. A., & Zheng, Y. (2016, jul). Robust and efficient insar deformation time series processing. In *2016 IEEE international geoscience and remote sensing symposium (IGARSS)*. IEEE. Retrieved from https://doi.org/10.1109/igarss.2016.7729827 doi: 10.1109/igarss.2016.7729827

Zheng, Y., & Zebker, H. A. (2017, jun). Phase Correction of Single-Look Complex Radar Images for User-Friendly Efficient Interferogram Formation. *IEEE Journal of Selected Topics in Applied Earth Observations and Remote Sensing*, *10*(6), 2694–2701. Retrieved from https://doi.org/10.1109/jstars.2017.2697861 doi: 10.1109/jstars.2017.2697861

Zwieback, S., Kokelj, S. V., Günther, F., Boike, J., Grosse, G., & Hajnsek, I. (2018, feb). Sub-seasonal thaw slump mass wasting is not consistently energy limited at the landscape scale. *The Cryosphere*, *12*(2), 549–564. Retrieved from https://doi.org/10.5194/tc-12-549-2018 doi: 10.5194/tc-12-549-2018